scientific reports

OPEN

Pyrite morphology and sulfur isotopes refine taphonomic models for the 2.1 Ga Francevillian biota, Gabon

Anna El Khoury[1,2], Farid Saleh[3✉], Abderrazak El Albani[1✉], Claude Fontaine[1], Claire Rollion-Bard[4], Ibtissam Chraiki[1], Jérémie Aubineau[5], Julie Ngwal'ghoubou Ikouanga[1], Mohamed Bhilisse[6], Maryem Zguaid[7], Andrea Somogyi[2] & Ernest Chi Fru[8]

Pyritization is a key taphonomic process that preserves some of Earth's oldest fossils. It is influenced by various factors such as organic matter type, the availability of iron and sulfur, and sedimentation rates. In this study, we analyzed pyritized biotic and abiotic structures from 2.1 Ga deposits in Gabon's Francevillian Basin, to reconstruct their taphonomic pathway at the micron scale. Using secondary ion mass spectrometry and scanning electron microscopy, we examine sulfur isotope compositions, pyrite morphology and grain size within individual fossils and compare them to abiotic pyritic concretions from the same stratigraphic level. Our results reveal differences in pyrite grain size and sulfur isotope composition between fossils and concretions. More importantly, chemical and morphological variations are observed within individual fossils, likely due to distinct reactive environments for pyrite mineralization, linked to organic matter, sulfate and iron availability during early diagenesis. This remarkable variation in pyrite morphology and $\delta^{34}S$ values in the fossilized specimens, indicates that they were compositionally more complex than the substrate that formed the homogeneously pyritized concretions. This well-preserved ecological window represents an exceptional record of the earliest multicellular life forms on Earth.

Authigenic mineralization is a key taphonomic process where soft tissues are replaced by minerals during decay, enhancing their preservation over geological time[1–4]. Common modes of soft tissue preservation include phosphatization[5,6], pyritization[7–9], and morphological replication and templating by aluminosilicate sheets[10–13], along with calcification and ferritization (i.e., preservation by iron oxides)[14,15]. Pyritization, in particular, is widespread and occurs in various depositional environments, such as in the Cambrian Burgess Shale and the Chengjiang Biota[8,16], the Ordovician Fezouata Biota[3,17,18] and Beecher's Trilobite Beds[19–21], the Cretaceous Brazilian and Lebanese Lagerstätten[22,23], and the Devonian Hünsruck Slate[19].

Biogenic pyrite nucleation, mainly attributed to microbial sulfate reduction during diagenesis[24], is driven by factors like organic matter content, sulfate availability, dissolved iron concentration, and pH[19,25–29]. Rapid sulfate reduction during early decay of labile organic matter promotes extensive pyrite nucleation, while slow decay delays it[8]. In iron-rich conditions, pyrite can replicate even non-labile structures through mineral substitution[1,19], as seen in the pyritized trilobite exoskeletons of the Beecher's Trilobite Beds[20,21]. However, sulfate availability can be limiting in certain situations, such as when deposition of carbonate cements on carcasses isolates specimens from seawater sulfates[29].

These complexities make it difficult to develop unified pyritization models in laboratory settings[30,31], leaving unresolved questions about post-mortem pyritization pathways that enable fossil preservation (e.g.[32,33], and references therein). Although advanced techniques like X-ray fluorescence, electron microscopy, and X-ray

[1]IC2MP, UMR 7285, CNRS, Université de Poitiers, 86073 Poitiers, France. [2]NANOSCOPIUM Beamline, Synchrotron SOLEIL, 91190 Saint-Aubin, France. [3]Institute of Earth Sciences, University of Lausanne, Géopolis, 1015 Lausanne, Switzerland. [4]Laboratoire des Sciences du Climat et de l'Environnement (LSCE), CNRS, CEA, UVSQ, Université Paris-Saclay, 91191 Gif-sur-Yvette, France. [5]Observatoire Midi-Pyrénées, Géosciences Environnement Toulouse, CNRS UMR 5563 (CNRS/UPS/IRD/CNES), Université de Toulouse, Toulouse, France. [6]Faculty of Sciences Semlalia, Cadi Ayyad University, Marrakech, Morocco. [7]Ecole des Mines de Paris, Paris, France. [8]School of Earth and Ocean Sciences, Cardiff University, Cardiff CF10 3AT, UK. ✉email: farid.nassim.saleh@gmail.com; abder.albani@univ-poitiers.fr

diffraction have been used to study fossil pyritization[7–9,16,22,33–37], the coupling of sulfur isotopes, organic matter, sulfate, and iron cycling to fossil preservation by pyritization remains underutilized.

Since their discovery, the biological affinity of the 2.1 Ga old Paleoproterozoic Francevillian macrofossils[38,39] continues to be debated[40,41], despite recent morphological, mineralogical, environmental and geochemical analyses, collectively pointing to a multicellular and eukaryotic affinity[38,42–48]. This pushback has arisen primarily because of the pyritized nature of some specimens, leading to suggestions that they may be artifacts of inorganic pyrite concretion.

Here, using electron microscopy and secondary ion mass spectrometry (SIMS), we sample pyritized macrofossils[38] and abiotic pyritized concretions from the Francevillian sub-basin to help settle this ongoing debate. We provide high-resolution evidence coupling post-mortem organic matter decay to biomass pyritization, by specifically associating unique pyrite morphologies to sulfur isotope distribution in the lobate macrofossils compared to the abiotic concretions sampled from the same stratigraphic layer. Collectively, the data enable micron-scale empirical modelling of the taphonomic processes that led to the pyritization and preservation of the lobate macrofossils. Their simple and broadly homogeneous structures allow the development of a robust pyritization model that enhances our understanding of their biogenicity and pyrite formation during early and late-stage diagenesis.

Results
Pyrite typology
The pyritized lobate macrofossils from the Francevillian basin consist of an ovoidal inner core, "the dome" and an outer succession of smaller lobes delimited by "radial fabrics" (Fig. 1a). These lobate fossils are typically composed of two distinct pyrite patterns. The dome shows dense and coarse euhedral crystals with some visible fractures (Fig. 1c,d). The radial fabrics are less dense (Fig. 1e–h) and consist of dispersed pyrite grains embedded in a black shale matrix (Fig. 1i). The dome, although densely populated with pyrite, exhibits a clear evolution in pyrite grain size with smaller pyrite grains gradually coagulating to form massive pyrites at the edges (Fig. 1j,k). On the other hand, the concretions consist of pyrite aggregates of no particular shape or size (Fig. 1b), occurring as isolated clusters of anhedral minerals welded into irregular shapes (Fig. 1l,m). Overall, the size and shape of pyrite crystals in these concretions are indistinguishable (Fig. 1n) compared to the distinct morphologies and size range observed in the lobate specimens (Fig. 1e–i).

Sulphur isotopes
The lobate fossils show $\delta^{34}S$ values ranging from − 30.7 to 52.7‰ that vary with pyrite shape and grain size (Fig. 2a–d; Supplementary Table S1). The $\delta^{34}S$ values in the radial fabrics are the most negative in the entire dataset, and together with their homogeneous distribution are distinctively associated with small euhedral pyrite crystals. They form a sharp dovetail or v-shaped groove that abuts smoothly with the narrower and tapering edge of the massive pyrite grains containing the most positive $\delta^{34}S$ values emerging from the central dome (Fig. 2a,c). The distinct pyrite morphologies and $\delta^{34}S$ signatures suggest that the dome and the radial fabrics are compositionally different. This is highlighted by vertical transects in the dome showing relatively higher $\delta^{34}S$ values compared to pyrite in the radial fabric and at the center of the dome (Fig. 3, Fig. S1; Supplementary Table S1). Moreover, negative $\delta^{34}S$ values at the dome's core progressively become more positive toward the edges (Fig. 2a–d), pointing to further compositional differentiation within the dome. The abiotic concretions, on the other hand, manifest positive $\delta^{34}S$ values ranging from 7.0 to 19.1‰ and averaging ~ 13.0‰ (Fig. 2e,f; Fig. S2). Both the dome's edges and the concretions contain mainly positive $\delta^{34}S$ values, with the most positive values in the dataset recorded at the dome's edges (Fig. 3; Supplementary Table S1).

Discussion
Pyrite differences between fossils and abiotic concretions
The results obtained show that pyrite shape, size, and sulfur isotopic ($\delta^{34}S$) compositions are different between the fossils and abiotic concretions. The presence of relatively small euhedral pyrite crystals in the fossils containing negative $\delta^{34}S$ values indicates an onset of rapid pyritization during early-stage diagenetic oxidation (decay) of labile-easy-to-degrade organic matter (OM) by sulfate-reducing microorganisms (SRM)[44,49–51], in the presence of abundant pore water sulfate and ferrous iron (Fe^{2+}), required for early, rapid pyrite precipitation[52]. Similar isotopic values are widely reported in the literature and are commonly found in well-conserved pyritized fossils[53,54]. On the other hand, the positive $\delta^{34}S$ values in the concretions and at the dome's edges suggest pyritization occurred under late-stage, lower-sulfate, and ^{34}S-enriched diagenetic conditions[44,55], mainly due to the distinct OM identity but also to the limited availability of sulfate in Proterozoic seawater[56]. The concretions likely formed through sulfate-dependent microbial oxidation of refractory OM in the pore water. This OM, which likely escaped oxidation in the water column, and potentially bound to iron oxides, underwent pyritization in low-sulfate, ^{34}S-enriched fluids during late-stage diagenesis[48]. This contrasts with the negative $\delta^{34}S$ values in the radial fabrics and at the center of the dome—a signature associated with rapid early-stage diagenetic oxidation of abundant and more labile OM in the presence of high dissolved sulfate concentration[52,57]. In this sense, the higher positive $\delta^{34}S$ values at the dome's edges compared to the concretions are consistent with complete pyritization of the dome long after the concretions were formed. This is corroborated by X-ray fluorescence (XRF) and X-ray Absorption Near Edge structure (XANES) data suggesting that pyrite in fossils nucleated mostly through arsenic-association during early diagenesis, which contrasts with abiotic concretions[58].
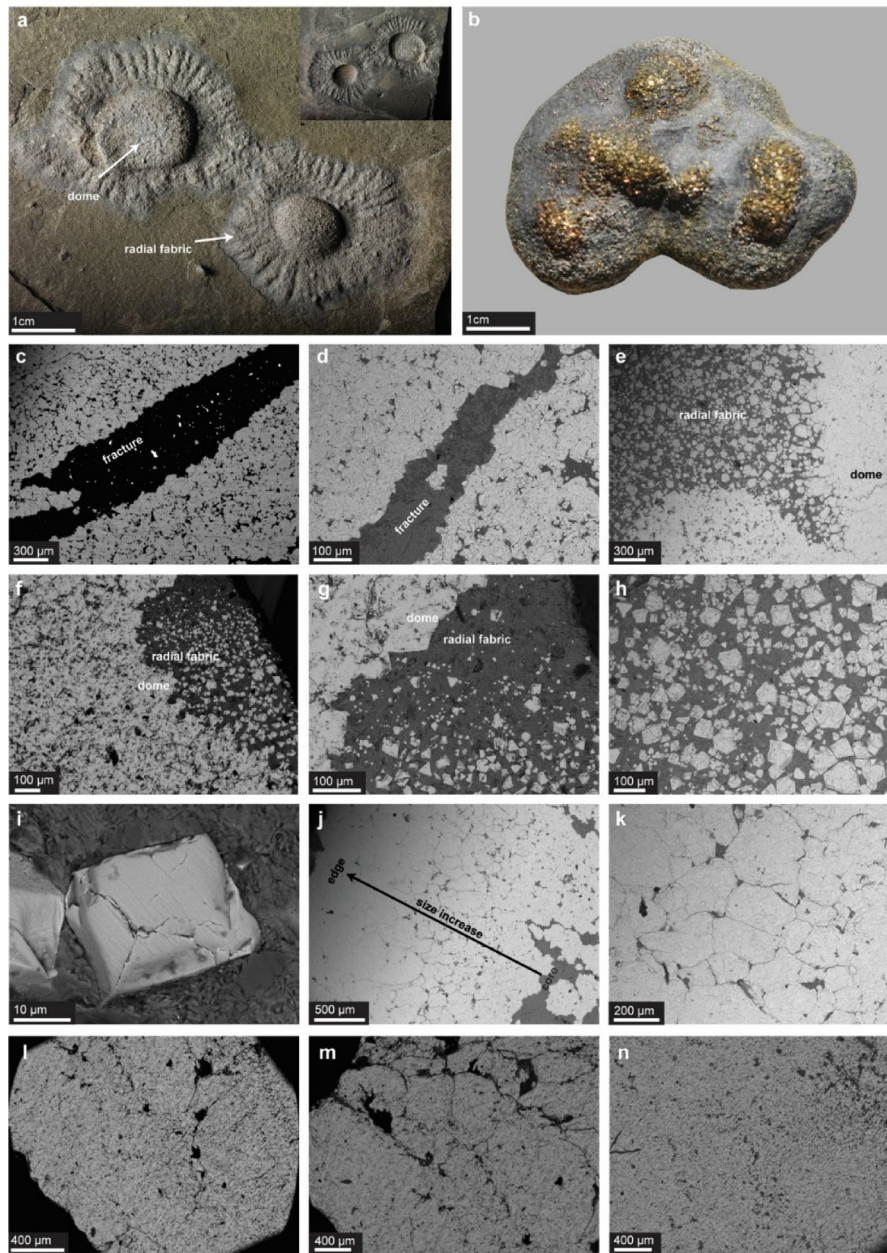
Fig. 1. Pyritization patterns in fossils and abiotic concretions. (**a**) Lobate fossils are composed of a central dome and radial fabric at the edges. **b.** Abiotic concretions show millimetric pyrite grains. (**c,d**) The center of the dome contains coagulated pyrite grains and many fractures. (**e,f,g**) The interface between the dome and the radial fabric is marked by a change in pyrite grain size and distribution. (**h**) Small euhedral pyrites of around 30 μm in size (**i**) are found in radial fabrics. **j.** A clear pyrite size evolution is noticed in the dome, going from the center outwards, with pyrite reaching 300 μm at the border (**k**). (**l,m,n**) Pyrite grains in the concretion are massive with no specific shapes.

Pyrite differences between the radial fabrics and the dome

Morphological and isotopic differences are not only observed between the fossils and abiotic concretions, but many heterogeneities in size, shape, and isotopic composition are recorded within the different compartments of the individual fossils, particularly within the dome and the radial fabrics (Figs. 1, 2 and 3). These observed heterogeneities could be explained by the structure and composition of OM[53]. The distribution of the $\delta^{34}S$ values is consistent with sulfate-dependent microbial oxidation of OM progressing sequentially from the radial fabrics to the dome's core, before terminating at the dome's edges, following the principles of closed system Rayleigh distillation of sulfur isotopes[59–61]. Accordingly, the data indicate that the dome likely contained a higher OM content than the radial fabrics, as suggested by the size increase and density of pyrite grains and decreasing $\delta^{34}S$ values from the radial fabrics into the dome's core. The highly negative $\delta^{34}S$ values and smaller pyrite
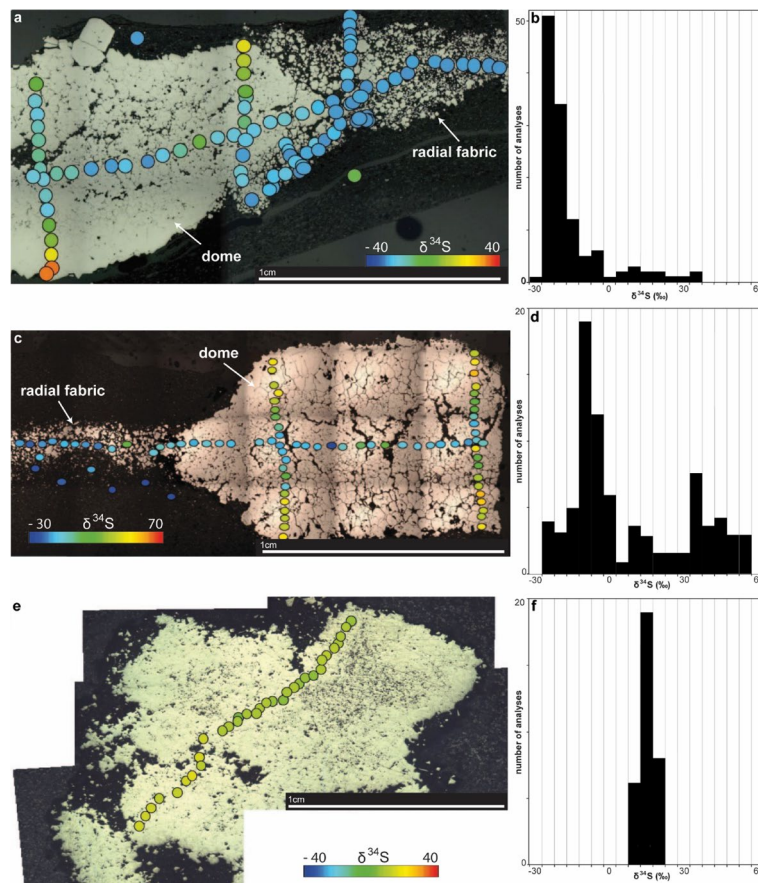
Fig. 2. Sulfur isotope data on fossils and abiotic concretions. Spatial δ^{34}S analyses on two lobate fossils (**a,c**), and related histograms showing the distribution of these isotopic data (**b,d**). Spatial δ^{34}S analyses on the abiotic concretion (**e**), and corresponding histogram (**f**). Note that the δ^{34}S data are heterogeneous within the fossils, but homogenous in the abiotic concretion.

crystals in the radial fabrics compared to the dome's core, align with precipitation during sulfate-replete early-stage diagenetic conditions. They also indicate that the lability (easy to decay) of OM may have decreased from the radial fabrics into the dome's core. This is because high-sulfate/high labile OM conditions promote rapid oxidation of OM by the SRMs, leading to the incorporation of light ^{32}S into rapidly precipitated authigenic pyrite[31,59,62]. This would produce a δ^{34}S fractionation gradient of lower δ^{34}S values in the radial fabrics relative to the dome's core, if they contained distinct OM that degraded at different rates in fluids containing different sulfate concentrations. For example, while the δ^{34}S values in the dome's core are also negative, they are generally higher compared to the radial fabrics, suggesting precipitation from lower sulfate fluids enriched in heavy ^{34}S. The more positive δ^{34}S signature at the dome's edges suggests precipitations from fossilization fluids containing the lowest sulfate concentrations and the most enriched ^{34}S composition.

Ruling out taphonomic artifacts as the origin of the preserved fossils

Previously, some suggested that the fossils could present preservation artifacts resulting from the growth of abiotic structures like pyrite suns. However, with the new data, it is clear that the fossils are distinct from pyrite suns, which exhibit a systematic growth pattern, with small, densely packed crystals forming at the center and larger, elongated, spaced-out crystals growing outward[38,44], creating their radial, sunburst structure. This pattern is thought to result from nucleation in confined conditions at the center, followed by growth and expansion on the outside[63,64]. They are suggested to originate from spherical framboidal pyrite precursors in monosulfide supersaturation conditions[63,64], with an increase in size and grain elongation correlating with the direction of crystal growth[38,44]. In contrast, the fossils show a different pyrite growth pattern from pyrite suns. The crystals do not elongate and enlarge from the inside to the outside—the smallest grains are in the outermost radial fabric, a location which should ideally correspond to where the largest grains in pyrite suns should be. Moreover, the largest pyrite grains in the fossils are instead encountered where intermediate crystals are expected in pyrite suns, that is, toward the edge of the dome. Pyrite suns grow radially outwards. Our data suggest that pyrite growth in the fossils occurred in discrete locations.

Moreover, from an isotopic perspective, the fossils have different isotopic compositions than pyrite sun models. Pyrite sun growth[63,64] happens in a closed system where sulfate becomes increasingly limiting over time, and a systematic increase in δ^{34}S values from the centre to the outer edges would be expected with pyrite
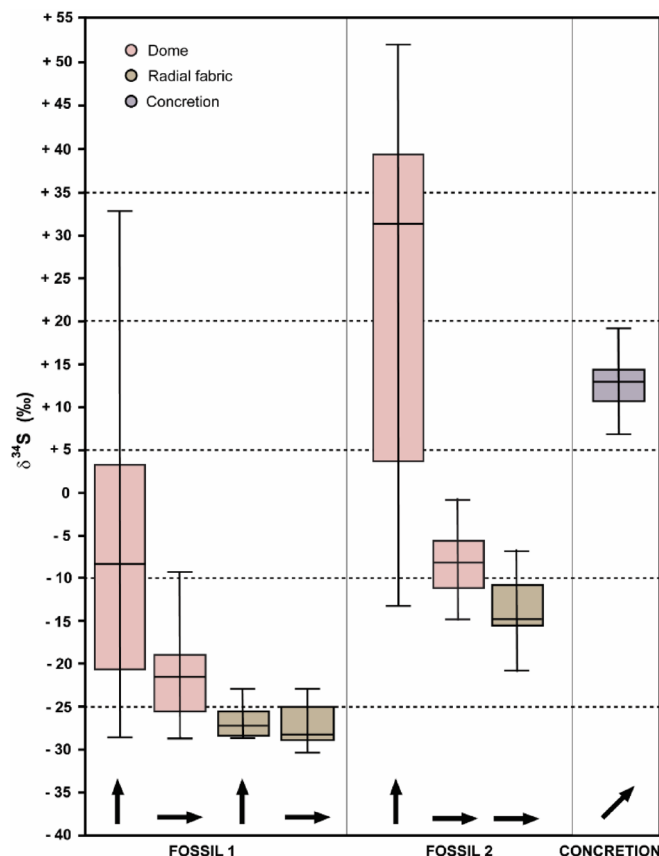
Fig. 3. Boxplots of $\delta^{34}S$ variability between fossils and abiotic concretions and within fossils. Values of $\delta^{34}S$ vary between the vertical and longitudinal transects of two lobate pyritized fossils and between the dome and the radial fabric within each fossil. These $\delta^{34}S$ values are also different from those observed on a diagonal transect in the abiotic concretion.

overgrowth[59]. In this respect, both pyrite suns and the fossils exhibit negative sulfur isotopes in their cores, consistent with microbial sulfate reduction during early-stage diagenesis. However, in close system conditions, the middle regions of pyrite suns should reveal intermediate $\delta^{34}S$ values, with the highest located at the outermost edges, controlled by systematic pyrite overgrowth. This is not the pattern observed in the fossils. Instead, the highest $\delta^{34}S$ values are found near the edges of the fossil's central dome, while the lowest occur in the outermost radial fabrics. Additionally, $\delta^{34}S$ analysis reveals no significant isotopic variation in Carboniferous and Jurassic pyrite sun[38,44]. In summary, pyrite suns should hypothetically display a closed system increase in $\delta^{34}S$ values from the core to its extremities or no increase if formed in an open or sulfate-rich environment. The fossil $\delta^{34}S$ values[38,44] do not follow these trends. The observed pyrite morphologies and grain sizes in fossils suggest that they are different from pyrite suns. Moreover, the unique morphological and isotopic composition of the co-eval concretions invalidates the possibility that the radial fabrics are an expression of late-stage diagenetic fluid modification, as they share no similarity.

Environment for pyrite precipitation

The Francevillian macrofossils lived in a shallow oxic environment and were buried and preserved in black shales[65–68]. During burial, sulfur cycling in organic-rich settings increases in complexity, resulting in difficulties in unravelling the specific processes responsible for pyrite precipitation. For instance, thermochemical sulfate reduction (TSR) could potentially account for the extreme $\delta^{34}S$ values if residual sulfate is preserved following high burial temperatures[69]. However, multiple lines of evidence argue against a significant TSR contribution in our samples. Firstly, the $\delta^{34}S$ data, when considered alongside primary pyrite morphology and geochemical signatures, support a predominantly microbial origin for pyrite precipitation. The absence of metamorphic overprinting further indicates that the sampled specimens have not been subjected to the elevated temperatures and pressures necessary to drive extensive TSR reactions[45,66,70,71]. Secondly, both the analyzed fossils and concretions lack residual sulfate, the key substrate of high $\delta^{34}S$ values in TSR-influenced samples[69]. This is because the quantitative reduction of sulfate results in the loss of the extreme $\delta^{34}S$ values produced by TSR reactions. Moreover, evidence from bulk acid extractable sulfate in the correlative Lastourville sub-basin shows that sulfate in the Franceville Group is limited and secondary in origin, arising from later pyrite oxidation[72]. For instance, inorganic sulfates are confined to veinlets, microfractures parallel to bedding planes and lining pyrite aggregates in some instances[72]. High-resolution SEM analysis revealed no evidence of similar morphological

features, pyrite oxidation and weathering in our samples. Taken together, these observations instead support a diagenetic microbial origin for the pyrites and concretions, rather than TSR.

We also find no strong evidence that recrystallization significantly affected the studied pyrites. The δ^{34}S signatures remain heterogeneous and vary with pyrite crystal size, which would not be the case if extensive recrystallization had occurred, otherwise, homogenized δ^{34}S values and uniform crystal morphologies would be expected instead. Our findings align with those of Paiste et al.[72], in which they observed limited pyrite recrystallization and preserved primary δ^{34}S signals in the equivalent Lastourville sub-basin of the Francevillian Group.

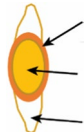## Model for pyrite precipitation and fractionation of sulfur isotopes

Considering all the above, a closed system model, marked by limiting sulfate conditions, starting with pyrite nucleation at the core of the specimens, terminating at the extremities, cannot solely explain the distribution of our data. Otherwise, the pyrite grains should elongate and enlarge from the core outwards and their corresponding δ^{34}S values should increase in the same direction. Instead, a most parsimonious explanation for the coupling of the δ^{34}S in the distinct pyrite morphologies associated with the fossils points to varying degradation rates of OM. They indicate that decomposition began with the radial fabrics, followed by the dome's core, before terminating at its edges. In this model, the entire specimen was exposed to the fossilization media at the onset of diagenesis, but pyritization of the individual parts was controlled primarily by OM content and composition. In this scenario, the most labile OM in the radial fabric was first degraded rapidly during early diagenesis, producing the most negative δ^{34}S values, consuming ^{32}S from the fossilization media to produce small pyrite crystals. This was then followed by the dome's core and then its edges as a response to OM lability and concentration. Such conditions would have resulted in slower OM degradation rates, proceeding from the dome's core to its edges. These later diagenetic conditions promoted the formation of the observed increase in pyrite crystal size and their increasingly more positive δ^{34}S composition, under increasing sulfate-limiting conditions, compared to the radial fabrics. This is because rapid OM oxidation by SRMs during an early non-sulfate limiting diagenetic scenario is expected to produce small-size pyrite crystals, while slower oxidation rates promote slower-more orderly growth and enlargement of pyrite[28,52,73,74].

Thus, the pyritization model indicates that the dome and the radial fabrics behaved as separate systems. In other words, despite being parts of the same organism, OM from the dome and radial fabrics did not decay at the same rate during diagenesis. While the radial fabrics and the dome's core contained low-density (labile) OM (LDOM) that decayed rapidly during burial, causing a high ^{32}S fractionation and negative δ^{34}S values, the more refractory high-density OM (HDOM) present in the dome's edges decayed slowly after burial, manifesting increasing δ^{34}S values characteristic of sulfate-limiting fluids (Table 1). The latter case is also valid for the late-stage diagenetic pyritization of the concretions due to the slow decay of free diffuse OM (DOM) or bounded to iron oxides in the pore water/sediments (Table 1) as suggested previously.

This is an unexpected scenario since no clear physical barriers separate the dome and the radial fabrics or show compartmentalization of the dome. The time-dependent oxidation of OM during diagenesis, which varies across different parts of the organism, points to a combination of factors: multiple mineralization fronts, sequential Rayleigh distillation processes allowing access to fluids with varying sulfate concentrations and δ^{34}S compositions, and oxidation of OM with differing levels of lability and resistance to decay[75]. This led to varying rates and duration of ^{32}S fractionation between the radial fabrics, the dome's inner and outer tissues in the lobate fossils, as well as in the concretions, all sampled from the same stratigraphic level (Fig. 4).

Implications

The mineralization front where iron from the environment meets sulfides and where pyrite starts to precipitate, indicates that if iron was scarce in the environment, sulfides would have migrated in search of iron, leading to pyrite precipitation away from the sites of OM oxidation. However, the distinct mineralization of structures, compared to the concretions, suggests a faithful spatial preservation of the morphologies of individual specimens, resulting in high-fidelity replication of features and organic composition. In the case of the investigated fossils, based on iron isotope studies on pyrites from the Francevillian fossils, the depositional environment was highly reactive, evidenced by negative δ^{56}Fe isotope values attributed to dissimilatory iron reduction (DIR) and kinetic iron isotope fractionation[48]. These favorable conditions that would have further released Fe^{2+} for pyrite

Organic matter				Degradation		Sulfur	
Type	Spatial distribution		Density	Condition	Duration	^{32}S fractionation	δ^{34}S
Benthic (Achritarchs)	Dispersed in sediment		DOM	After burial	Long	Low	+
Nereic (Multicellular organisms)	Located in the bottom		HDOM	After burial	Long	High => low	From – to +
			LDOM	During burial	Short	High	–
			LDOM	During burial	Short	High	–

Table 1. Comparison of the parameters of pyritization between concretions and lobate fossils. *DOM* diffuse organic matter, *HDOM* high-density organic matter, *LDOM* Low- density organic matter.
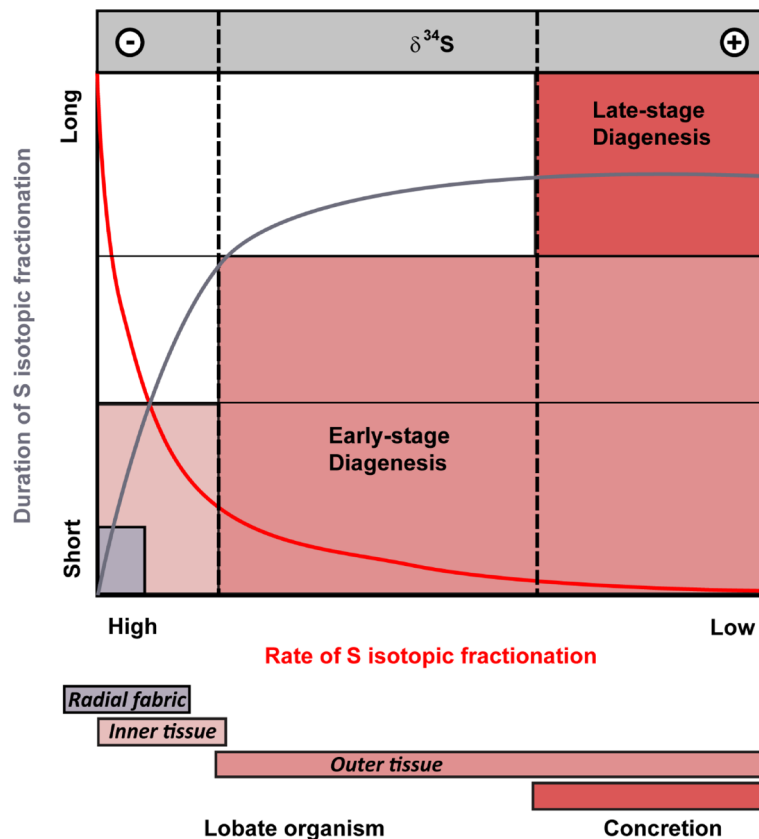
Fig. 4. Evolution of the sulfur isotopic fractionation (rate, duration) during the pyritization of the lobate fossils and concretions.

nucleation, likely led to the immediate precipitation of pyrite as soon as sulfides were formed, preventing their migration within the system.

In brief, the pyritized replicas of these organisms, despite their simple morphology, show a complex process reliant on differences in OM concentration, type and accessibility between the dome and the radial fabrics. This subtle complexity resulted in a complex time-dependent post-mortem decay process that produced distinct mineralization patterns corresponding to organic composition (e.g., concentration and lability) of individual parts of the organism (Fig. 5). The recurrent dovetail fitting of the smaller negative $\delta^{34}S$ radial fabric pyrite grains into the larger highly positive $\delta^{34}S$ pyrites at the dome's edge, suggest the dome was likely composed of a type of OM that was more resistant to degradation compared to the radial fabrics. Hence, the data suggest that the dome's edges potentially provided an anchoring surface for the radial fabrics. This more resistant ring also protected the dome's core, which, as suggested by its lower $\delta^{34}S$ values and smaller pyrite crystal grains compared to the edges, contained a type of OM that was less resistant to degradation, further highlighting the complexity of these organisms.

Detailed petrographic and isotopic data at the micron scale, comparing pyritized macrofossil specimens and abiotic concretions, provide unique and valuable insights into the mechanisms underlying the preservation of the 2.1-billion-year-old lobate fossils in the Paleoproterozoic Francevillian Sub-basin. Variations in pyrite size and their associated $\delta^{34}S$ values within the same fossil, compared to fossil concretions from the same layer, reveal contrasting pyritization mechanisms, influenced by OM, iron, and sulfate availability. Taken together, the heterogeneities of pyrite morphologies and associated $\delta^{34}S$ compositions in the fossil specimens, suggest they were compositionally more complex compared to the substrate from which the pyritized concretions formed. The latter shows no variability in pyrite morphology and mainly contains positive $\delta^{34}S$ values. This highlights the complexity of these organisms and their importance in understanding some of the earliest traces of life on Earth.

Methods
Hundreds of samples were collected from the FB2b black shale subunit of the Francevillian formation including lobate multicellular eukaryotes, as well as abiotic pyritized concretions. Selected polished sections of five lobate fossils (LV1, AG1L, AG2L, AG3L, AG4) and 3 concretions (Conc-G1, Conc-G2, CH-1) were carbon-coated and examined using JEOL JSM IT500 Scanning Electron Microscope at the University of Poitiers, France (HT = 15 kV, WD = 11 mm, PC = 1nA). The scanning electron microscopy instrument was equipped with secondary electron and backscatter electron detectors.
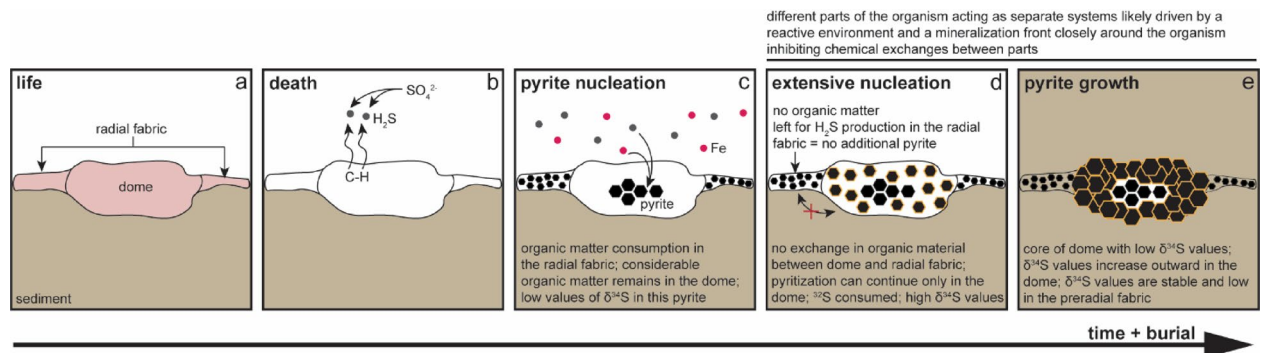
Fig. 5. Conceptual pyritization model for the lobate fossils. (**a**) The lobate fossil is composed of a central dome and radial fabrics at the edges. (**b**) After death, decay proceeds releasing organic material and leading to the reduction of sulfates from seawater into sulfides. (**c**) Sulfides react with available iron leading to pyrite nucleation in radial fabrics and the center of the dome. (**d**) Pyrite nucleation continues exclusively where organic matter is not fully consumed (to reduce sulfates), mainly at the border of the dome, but this pyrite has a different isotopic composition from the previously precipitated one since light sulfur has been already consumed. (**e**) Pyrite growth occurs where organic material is still available at the outermost part of the dome (where iron from the environment is also available). The growth of pyrite at the borders eventually isolates the pyrite at the center of the dome from the external environment, prohibiting its further growth and resulting in an increase of pyrite grain size from the center going outward of the dome.

Sulfur isotopes ($^{34}S/^{32}S$ ratio) were measured on 95 and 80 pyrite grains in two lobate specimens and on 33 pyrite grains in a concretion using Secondary Ion Mass Spectrometry (SIMS) Cameca IMS1270 and 1280 instruments at Centre de Recherches Pétrographiques et Géochimiques (CRPG, Nancy, France). The samples were embedded in epoxy then polished with polishing mats and diamond paste down to 1 μm to avoid artifacts linked to the samples' topography. DFTA values stayed in the deflector range confirming the rigorous control of samples polishing. Same analytical conditions were used as in previously described work[76]. The sulfur isotopic compositions were measured using a 15 μm Cs^+ primary beam of < 2–5 nA. Sulfur isotopes were measured in a multi-collector mode using two off-axis Faraday cups (L'2 and H'1). The gains of the Faraday cups were inter-calibrated at the beginning of the analytical session and the offsets were determined before each analysis during the pre-sputtering (300 s). Typical ion intensities of 3×10^9 counts per second (cps) were obtained on $^{32}S^-$, so that an internal error better than 0.1‰ was reached. Instrumental mass fractionation and external reproducibility were determined by multiple measurements of the in-house reference materials Pyr3B ($\delta^{34}S = + 1.41‰$), Maine ($\delta^{34}S = - 20.61‰$), Balmat ($\delta^{34}S = + 15.1‰$) and Spain ($\delta^{34}S = - 2.95‰$). The external reproducibility ranged between 0.10 and 0.40% (1 σ), depending on the analytical session. FC backgrounds and yields corrections, as well as IMF corrections were applied for the measurements. No matrix effect nor drift were detected during analytical sessions. Measurements for each spot were examined for contamination (due to the presence of cracks) and values were not used when it was the case. For an inter-comparison of results between SIMS platforms and between in situ techniques, some of the samples were measured by another SIMS platform (NorSIMS) and by laser ablation at IFREMER Brest. All showed same range in isotopic compositions.

Data availability
All data necessary for the replication of this study is available in the main text or the supplementary dataset.

References
1. Briggs, D. E. G. The role of decay and mineralization in the preservation of soft-bodied fossils. *Annu. Rev. Earth Planet. Sci.* **31**, 275–301 (2003).
2. Purnell, M. A., Zhang, M., Jiang, H. & Lai, X. Reconstruction, composition and homology of conodont skeletons: A response to Agematsu et al.. *Palaeontology* **61**, 793–796 (2018).
3. Saleh, F. et al. Insights into soft-part preservation from the early ordovician Fezouata Biota. *Earth Sci. Rev.* **213**, 103464 (2021).
4. Corthésy, N., Antcliffe, J. B. & Saleh, F. Taxon-specific redox conditions control fossilisation pathways. *Nat. Commun.* **16**, 3993 (2025).
5. Briggs, D. E. G., Kear, A. J., Martill, D. M. & Wilby, P. R. Phosphatization of soft-tissue in experiments and fossils. *JGS* **150**, 1035–1038 (1993).
6. Gueriau, P. et al. Oxidative conditions can lead to exceptional preservation through phosphatization. *Geology* **48**, 1164–1168 (2020).
7. Farrell, Ú. C. Pyritization of soft tissues in the fossil record: An overview. *Paleontol. Soc. pap.* **20**, 35–58 (2014).
8. Gabbott, S. E., Xian-guang, H., Norry, M. J. & Siveter, D. J. Preservation of early Cambrian animals of the Chengjiang biota. *Geology* **32**, 901 (2004).
9. Ma, X., Edgecombe, G. D., Hou, X., Goral, T. & Strausfeld, N. J. Preservational pathways of corresponding brains of a Cambrian euarthropod. *Curr. Biol.* **25**, 2969–2975 (2015).

10. Anderson, R. P., Tosca, N. J., Saupe, E. E., Wade, J. & Briggs, D. E. G. Early formation and taphonomic significance of kaolinite associated with Burgess Shale fossils. *Geology* **49**, 355–359 (2021).

11. Corthésy, N., Saleh, F., Antcliffe, J. B. & Daley, A. C. Kaolinite induces rapid authigenic mineralisation in unburied shrimps. *Commun. Earth Environ.* **6**, 4 (2025).

12. Orr, P. J., Briggs, D. E. G. & Kearns, S. L. Cambrian burgess Shale animals replicated in clay minerals. *Science* **281**, 1173–1175 (1998).

13. Corthésy, N., Saleh, F., Thomas, C., Antcliffe, J. B. & Daley, A. C. The effects of clays on bacterial community composition during arthropod decay. *Swiss J. Palaeontol.* **143**, 26 (2024).

14. Chraiki, I. et al. A 571 million-year-old alkaline volcanic lake photosynthesizing microbial community, the Anti-atlas, Morocco. *Geobiology* **19**, 105–124 (2021).

15. Chraiki, I., Bouougri, E. H. & El Albani, A. Microbialites diversity from the Ediacaran of the anti-atlas (Morocco): A snapshot of microbial oases thriving in an alkaline volcanic lake. *Ann. Paléontol.* **108**, 102584 (2022).

16. Lei, X., Cong, P., Zhang, S., Wei, F. & Anderson, R. P. Unveiling an ignored taphonomic window in the early Cambrian Chengjiang Biota. *Geology* **52**, 753–758 (2024).

17. Saleh, F. et al. Skeletal elements controlled soft-tissue preservation in echinoderms from the early Ordovician Fezouata Biota. *Geobios* **81**, 51–66 (2023).

18. Saleh, F. et al. Taphonomic bias in exceptionally preserved biotas. *Earth Planet. Sci. Lett.* **529**, 115873 (2020).

19. Raiswell, R. A geochemical framework for the application of stable sulphur isotopes to fossil pyritization. *JGS* **154**, 343–356 (1997).

20. Briggs, D. E. G., Bottrell, S. H. & Raiswell, R. Pyritization of soft-bodied fossils: Beecher's trilobite bed, upper ordovician, New York State. *Geology* **19**, 1221 (1991).

21. Farrell, U. C., Briggs, D. E. G. & Gaines, R. R. Paleoecology of the Olenid Trilobite Triarthus: New evidence from Beecher's trilobite bed and other sites of pyritization. *Palaios* **26**, 730–742 (2011).

22. Barling, N., Saleh, F. & Ma, X. A unique record of prokaryote cell pyritization. *Geology* **51**, 1062–1066 (2023).

23. George, H. et al. The famous fish beds of lebanon: The upper cretaceous Lagerstätten of Haqel, Hjoula, Nammoura and Sahel Aalma. *JGS* **181**, jgs2023-210 (2024).

24. Mansor, M et al. Biogenic pyrite and metastable iron sulfides: Emerging formation pathways and geological and societal relevance. *Geo-bio interfaces* **2**, e6 (2025).

25. Berner, R. A. Sedimentary pyrite formation. *Am. J. Sci.* **268**, 1–23 (1970).

26. Huerta-Diaz, M. A. & Morse, J. W. Pyritization of trace metals in anoxic marine sediments. *Geochim. Cosmochim. Acta* **56**, 2681–2702 (1992).

27. Raiswell, R. & Canfield, D. E. Sources of iron for pyrite formation in marine sediments. *Am. J. Sci.* **298**, 219–245 (1998).

28. Sim, M. S., Ono, S., Donovan, K., Templer, S. P. & Bosak, T. Effect of electron donors on the fractionation of sulfur isotopes by a marine Desulfovibrio sp. *Geochim. Cosmochim. Acta* **75**, 4244–4259 (2011).

29. Gaines, R. R. et al. Mechanism for Burgess shale-type preservation. *Proc. Natl. Acad. Sci. U.S.A.* **109**, 5180–5184 (2012).

30. Grimes, S. T. et al. Understanding fossilization: Experimental pyritization of plants. *Geology* **29**, 123 (2001).

31. Odin, G. P., Leloup, J., Nguyen Tu, T. T., Charbonnier, S. & Derenne, S. Taphonomic experiments on caridean shrimp elucidate the timing and influence of organic matter on diagenetic pyritization and sulfurization. *Chem. Geol.* **644**, 121858 (2024).

32. Janssen, K., Mähler, B., Rust, J., Bierbaum, G. & McCoy, V. E. The complex role of microbial metabolic activity in fossilization. *Biol. Rev.* **97**, 449–465 (2022).

33. Saleh, F., Daley, A. C., Lefebvre, B., Pittet, B. & Perrillat, J. P. Biogenic Iron preserves structures during fossilization: A hypothesis: Iron from decaying tissues may stabilize their morphology in the fossil record. *BioEssays* **42**, 1900243 (2020).

34. Saleh, F. et al. Iron from continental weathering dictated soft-part preservation during the Early Ordovician. *Terra Nova* **34**, 163–168 (2022).

35. Saleh, F., Pittet, B., Perrillat, J.-P. & Lefebvre, B. Orbital control on exceptional fossil preservation. *Geology* **47**, 103–106 (2019).

36. Schiffbauer, J. D. et al. A unifying model for Neoproterozoic-Palaeozoic exceptional fossil preservation through pyritization and carbonaceous compression. *Nat. Commun.* **5**, 5754 (2014).

37. Zhu, M., Babcock, L. E. & Steiner, M. Fossilization modes in the Chengjiang Lagerstätte (Cambrian of China): Testing the roles of organic preservation and diagenetic alteration in exceptional preservation. *Palaeogeogr. Palaeoclimatol. Palaeoecol.* **220**, 31–46 (2005).

38. El Albani, A. et al. Large colonial organisms with coordinated growth in oxygenated environments 2.1 Gyr ago. *Nature* **466**, 100–104 (2010).

39. Ikouanga, J. N. et al. The first application of Re–Os dating on Paleoproterozoic francevillian sediments (Gabon). *Comptes Rendus. Géosci.* **356**, 57–66 (2024).

40. Anderson, R. P., Tarhan, L. G., Cummings, K. E., Planavsky, N. J. & Bjørnerud, M. Macroscopic structures in the 1.1 Ga continental Copper Harbor formation: Concretions or fossils?. *Palaios* **31**, 327–338 (2016).

41. Fakhraee, M. et al. Earth's surface oxygenation and the rise of eukaryotic life: Relationships to the Lomagundi positive carbon isotope excursion revisited. *Earth Sci. Rev.* **240**, 104398 (2023).

42. El Albani, A. et al. A search for life in Palaeoproterozoic marine sediments using Zn isotopes and geochemistry. *Earth Planet. Sci. Lett.* **612**, 118169 (2023).

43. El Albani, A. et al. Organism motility in an oxygenated shallow-marine environment 2.1 billion years ago. *Proc. Natl. Acad. Sci. U.S.A.* **116**, 3431–3436 (2019).

44. El Albani, A. et al. The 2.1 Ga old Francevillian biota: Biogenicity, taphonomy and biodiversity. *PLoS ONE* **9**, e99438 (2014).

45. Ikouanga, J. N. et al. Taphonomy of early life (2.1 Ga) in the francevillian basin (Gabon): Role of organic mineral interactions. *Precambrian Res.* **395**, 107155 (2023).

46. Ossa Ossa, F. et al. Zinc enrichment and isotopic fractionation in a marine habitat of the c. 2.1 Ga Francevillian Group: A signature of zinc utilization by eukaryotes?. *Earth Planet. Sci. Lett.* **611**, 118147 (2023).

47. Chi Fru, E. et al. Hydrothermal seawater eutrophication triggered local macrobiological experimentation in the 2100 Ma Paleoproterozoic Francevillian sub-basin. *Precambr. Res.* **409**, 107453 (2024).

48. Ajagunjeun, A. A. et al. Expansion of the aerobic iron biogeochemical cycle during the Paleoproterozoic Lomagundi event. *Commun. Earth Environ.* **6**, 113 (2025).

49. Khan, D. et al. Genesis and distribution of pyrite in the lacustrine shale: Evidence from the Es3x shale of the Eocene Shahejie formation, Zhanhua Sag, East China. *ACS Omega* **7**, 1244–1258 (2022).

50. Köster, M. et al. Uniquely low stable iron isotopic signatures in deep marine sediments caused by Rayleigh distillation. *Sci. Rep.* **13**, 10281 (2023).

51. Wilkin, R. T., Barnes, H. L. & Brantley, S. L. The size distribution of framboidal pyrite in modern sediments: An indicator of redox conditions. *Geochim. Cosmochim. Acta* **60**, 3897–3912 (1996).

52. Habicht, K. S., Canfield, D. E. & Rethmeier, J. Sulfur isotope fractionation during bacterial reduction and disproportionation of thiosulfate and sulfite. *Geochim. Cosmochim. Acta* **62**, 2585–2595 (1998).

53. Guan, C. et al. Controls on fossil pyritization: Redox conditions, sedimentary organic matter content, and Chuaria preservation in the Ediacaran Lantian Biota. *Palaeogeogr. Palaeoclimatol. Palaeoecol.* **474**, 26–35 (2017).

54. Farrell, U. C., Briggs, D. E. G., Hammarlund, E. U., Sperling, E. A. & Gaines, R. R. Paleoredox and pyritization of soft-bodied fossils in the Ordovician Frankfort Shale of New York. *Am. J. Sci.* **313**, 452–489 (2013).

55. McKay, J. L. & Longstaffe, F. J. Sulphur isotope geochemistry of pyrite from the upper cretaceous Marshybank formation, western interior basin. *Sediment. Geol.* **157**, 175–195 (2003).
56. Fakhraee, M., Hancisse, O., Canfield, D. E., Crowe, S. A. & Katsev, S. Proterozoic seawater sulfate scarcity and the evolution of ocean–atmosphere chemistry. *Nat. Geosci.* **12**, 375–380 (2019).
57. Berner, R. A. Sedimentary pyrite formation: An update. *Geochim. Cosmochim. Acta* **48**, 605–615 (1984).
58. El Khoury, A. et al. A battle against arsenic toxicity by Earth's earliest complex life forms. *Nat. Commun.* **16**(1), 1–14 (2025).
59. Canfield, D. E. Biogeochemistry of sulfur isotopes. *Mineral. Geochem.* **43**(1), 607–636 (2001).
60. Seal, R. R. Sulfur isotope geochemistry of sulfide minerals. *Rev. Mineral. Geochem.* **61**, 633–677 (2006).
61. Johnston, D. T., Farquhar, J. & Canfield, D. E. Sulfur isotope insights into microbial sulfate reduction: When microbes meet models. *Geochim. Cosmochim. Acta* **71**, 3929–3947 (2007).
62. Duverger, A. et al. Mechanisms of pyrite formation promoted by sulfate-reducing bacteria in pure culture. *Front. Earth Sci.* **8**, 588310 (2020).
63. Merinero, R. & Cárdenes, V. Theoretical growth of framboidal and sunflower pyrite using the R-package frambgrowth. *Miner. Petrol.* **112**, 577–589 (2018).
64. Merinero, R., Cárdenes, V., Lunar, R., Boone, M. N. & Cnudde, V. Representative size distributions of framboidal, euhedral, and sunflower pyrite from high-resolution X-ray tomography and scanning electron microscopy analyses. *Am. Miner.* **102**, 620–631 (2017).
65. Canfield, D. E. et al. Oxygen dynamics in the aftermath of the great oxidation of earth's atmosphere. *Proc. Natl. Acad. Sci. U.S.A.* **110**, 16736–16741 (2013).
66. Ngombi-Pemba, L., Albani, A. E., Meunier, A., Grauby, O. & Gauthier-Lafaye, F. From detrital heritage to diagenetic transformations, the message of clay minerals contained within shales of the Palaeoproterozoic Francevillian basin (Gabon). *Precambr. Res.* **255**, 63–76 (2014).
67. Reynaud, J.-Y. et al. Depositional setting of the 2·1 Ga Francevillian macrobiota (Gabon): Rapid mud settling in a shallow basin swept by high-density sand flows. *Sedimentology* **65**, 670–701 (2018).
68. Aubineau, J. et al. Benthic redox conditions and nutrient dynamics in the ca. 2.1 Ga Franceville sub-basin. *Precamb. Res.* **360**, 106234 (2021).
69. Cai, C., Li, H., Li, K. & Wang, D. Thermochemical sulfate reduction in sedimentary basins and beyond: A review. *Chem. Geol.* **607**, 121018 (2022).
70. Bankole, O. M., El Albani, A., Meunier, A. & Gauthier-Lafaye, F. Textural and paleo-fluid flow control on diagenesis in the Paleoproterozoic Franceville Basin, South Eastern, Gabon. *Precamb. Res.* **268**, 115–134 (2015).
71. Gauthier-Lafaye, F., Holliger, P. & Blanc, P.-L. Natural fission reactors in the Franceville basin, Gabon: A review of the conditions and results of a "critical event" in a geologic system. *Geochim. Cosmochim. Acta* **60**, 4831–4852 (1996).
72. Paiste, K. et al. Sulfur isotopes from the Paleoproterozoic Francevillian Basin record multigenerational pyrite formation, not depositional conditions. *Commun. Earth Environ.* **5**, 328 (2024).
73. Lin, Z. et al. How sulfate-driven anaerobic oxidation of methane affects the sulfur isotopic composition of pyrite: A SIMS study from the South China Sea. *Chem. Geol.* **440**, 26–41 (2016).
74. Rickard, D. & Luther, G. W. Chemistry of Iron sulfides. *Chem. Rev.* **107**, 514–562 (2007).
75. Raiswell, R., Whaler, K., Dean, S., Coleman, M. L. & Briggs, D. E. G. A simple three-dimensional model of diffusion-with-precipitation applied to localised pyrite formation in framboids, fossils and detrital iron minerals. *Mar. Geol.* **113**, 89–100 (1993).
76. Thomassot, E. et al. Metasomatic diamond growth: A multi-isotope study (13C, 15N, 33S, 34S) of sulphide inclusions and their host diamonds from Jwaneng (Botswana). *Earth Planet. Sci. Lett.* **282**, 79–90 (2009).

Acknowledgements

Author contributions

Funding

Declarations

Competing interests

The authors declare no competing interests.

Additional information

Supplementary Information The online version contains supplementary material available at https://doi.org/10.1038/s41598-025-04512-4.

Correspondence and requests for materials should be addressed to F.S. or A.E.A.

Reprints and permissions information is available at www.nature.com/reprints.

Publisher's note Springer Nature remains neutral with regard to jurisdictional claims in published maps and institutional affiliations.